

Carbon Nanotubes in Helically Modulated Potentials

P. J. Michalski and E. J. Mele

Department of Physics and Astronomy, University of Pennsylvania, Philadelphia, PA 19104

(Dated: February 4, 2008)

We calculate effects of an applied helically symmetric potential on the low energy electronic spectrum of a carbon nanotube in the continuum approximation. The spectrum depends on the strength of this potential and on a dimensionless geometrical parameter, P , which is the ratio of the circumference of the nanotube to the pitch of the helix. We find that the minimum band gap of a semiconducting nanotube is reduced by an arbitrarily weak helical potential, and for a given field strength there is an optimal P which produces the biggest change in the band gap. For metallic nanotubes the Fermi velocity is reduced by this potential and for strong fields two small gaps appear at the Fermi surface in addition to the gapless Dirac point. A simple model is developed to estimate the magnitude of the field strength and its effect on DNA-CNT complexes in an aqueous solution. We find that under typical experimental conditions the predicted effects of a helical potential are likely to be small and we discuss several methods for increasing the size of these effects.

PACS numbers: 73.22.Dj, 73.43.Cd, 73.63.Fg

I. INTRODUCTION

In recent years it has become a common practice to functionalize CNTs with water soluble, high molecular weight, quasi-linear molecules such as synthetic polymers and DNA.^{1,2,3} These molecules bind to individual CNTs via van der Waals forces and form robust and stable complexes with the nanotube.⁴ The resulting complex is easily dispersed in an aqueous solution because the hydrophobic nanotube is screened from the water by the wrapping molecule, while the hydrophilic regions of the DNA or polymer are free to interact with the solvent. Forming such complexes between CNTs and quasi-linear molecules is the only known way to disperse nanotubes in aqueous media without using surfactants or chemically modifying the CNT. Several practical applications have been realized as a result of this technique. DNA wrapped CNTs can be sorted by diameter using density gradient ultra-centrifugation, and the resulting mixture filtered to obtain a solution comprised almost entirely of one nanotube species.⁵ DNA wrapped CNTs are especially well suited for biological applications, such as cellular markers,⁶ which are not possible with surfactant dispersed CNTs because surfactant molecules generally destroy biological systems.

Simulations and experimental observations indicate that polymers and DNA can wrap around the exterior of a CNT in an ordered, helical fashion.^{1,2,7,8,9} In this paper we will study the effect of a helical potential on the single particle energy spectrum of a CNT. From a practical perspective, such a calculation is needed because of the large number of experiments performed on DNA-CNT complexes and changes in the band structure induced by the helical potential must be taken into account when interpreting experimental data. Also, while many polymers easily dissociate from the nanotube upon a change in solvent,¹ DNA is much more difficult to remove.¹⁰ For device applications, it will be useful to know if a DNA-CNT complex can be substituted for a pristine CNT

without a change in response or loss of function. From a more fundamental perspective, our work provides scaling relationships relating changes in the band structure to structural parameters such as the nanotube radius and the pitch of the helix.

Two related studies have recently been published. In Ref. (11), the authors modeled the nanotube as a free electron gas confined to the surface of a cylinder and governed by the non-relativistic Schrodinger equation. A helical potential was introduced as a series of delta functions, similar to the Kronig-Penney model. This study concluded that the total electronic energy is an oscillatory function of the pitch, with several local minima indicating preferred wrapping angles. However, it has been shown that the low energy electronic structure of a CNT is better described by the Dirac Hamiltonian for a massless relativistic particle.^{12,13} While the results of Ref. (11) may describe the effect of a helical potential on a semiconducting nanowire, it does not generally describe the electronic physics of a carbon nanotube. Although we do not study the total electronic energy, our results below, obtained within the long wavelength Dirac theory, do not show any oscillatory behavior as a function of the pitch.

In Ref. (14), the authors studied the electronic response of an armchair nanotube to an applied helical potential. Only potentials commensurate with the nanotube lattice were considered, and the high symmetry of the underlying armchair lattice was important in facilitating calculations. This study concluded that the external potential opened up small band gaps in the originally metallic nanotube. To discover such an effect it is important to consider the nanotube lattice; as such, the continuum theory we develop below does not reproduce these tiny band gaps. To study a general chiral nanotube with an arbitrary helical potential using the method of Ref. (14) would be a formidable task, whereas the problem is accessible within the continuum theory. The trade-off is that we miss higher order effects such as tiny band

gaps in otherwise metallic nanotubes. In general the effects missed by the continuum theory are so small as to be unimportant. The corrections introduced by higher order considerations are discussed in the conclusion and in the two appendices.

For semi-conducting tubes, we find that the band gap always closes under an applied, arbitrarily weak helical potential. For a given polymer-CNT system, the change in the band gap is a relatively sharply peaked function of pitch, with an optimum pitch maximizing the response to the potential. As the pitch goes to zero, the effect of the helical potential vanishes. As the pitch goes to infinity, there are two different behaviors depending on the strength of the applied field: for weak fields the effect of the chiral potential vanishes, for strong fields the band gap remains closed. For metallic tubes, we find that the Fermi velocity is a slowly decreasing function of pitch. As with semi-conducting tubes, as the pitch goes to zero the effect of helical potential vanishes. As the pitch goes to infinity, there are again two different behaviors depending on the field strength. For strong fields two small gaps, inversely proportional to the pitch, appear near the Fermi surface in addition to the gapless Fermi point. For weak fields no such gaps appear in the spectrum. In both cases the Fermi velocity is reduced by the helical potential.

Early on it was conjectured that the underlying chirality of the CNT might determine the pitch of an adsorbed polymer¹⁵. However, it is now generally believed that the adsorbed species need not conform to the lattice structure of the nanotube. The structure of most wrapping molecules is actually incommensurate with the nanotube lattice, and deforming the molecule to match the lattice can be energetically unfavorable.¹⁶ Simulations show that, depending on the nucleotide base sequence, single stranded DNA (ssDNA) can wrap around a given nanotube in a left-handed or right-handed helix, or even bond linearly along the tube.^{2,4} Experiments show that identical strands of DNA will wrap with the same handedness around enantiomeric pairs of nanotubes.¹⁷ Additionally, recent simulations demonstrate that DNA bases can adhere to a nanotube in hundreds of stable configurations.¹⁸ All of this is strong evidence that the underlying lattice of the nanotube plays little to no role in determining the structure of the CNT-DNA (-polymer) complex. The evidence suggests that the DNA (polymer) wraps in a manner determined by its own physical properties (chemical composition, elastic stiffness, size, etc.) and the CNT radius.⁹ Furthermore, the interaction between the nanotube and the wrapping molecule should be adequately described by a position independent binding energy.¹⁶ These observations motivate us to ignore the discrete atomic nature of the nanotube and treat it as a cylinder in the continuum limit in our calculations below.

The remainder of this paper is organized as follows. In Sec. II we will describe our model and a convenient coordinate transformation. In Sec. III we will give analytic and numerical solutions of the low energy spectrum

for both metallic and semi-conducting tubes. In Sec. IV we use a simple model of the wrapping molecule to estimate the magnitude of the applied field and the resulting change in the nanotube band gap. In Sec. V we give a brief conclusion.

II. MODEL SYSTEM

As discussed in the introduction, the nanotube will be modeled as a continuous cylinder subjected to an external helical potential. By developing a long wavelength continuum theory we can avoid complications that arise when considering electrons subjected to two incommensurate potentials on the scale of the lattice constant.¹⁹ The low energy electronic states of the nanotube are obtained by expanding the graphene Hamiltonian around the \mathbf{K} and \mathbf{K}' points and applying appropriate boundary conditions.^{12,13} In what follows we consider the solutions near the \mathbf{K} point since the response to a static helical potential must be the same at \mathbf{K} and \mathbf{K}' due to time reversal symmetry.

A long wavelength continuum theory is appropriate if the pitch of the potential is large compared to the nanotube lattice spacing. Below we will investigate the electronic response of the nanotube as a function of the pitch of the potential and the nanotube circumference. The important parameter will be the ratio of circumference to pitch, and we will study the response of the nanotube in the limits that this ratio goes to zero and as it goes to infinity. In the first limit we imagine fixing the nanotube radius and allowing the pitch to go to infinity, where our long wavelength description is certainly valid. In the second limit the long wavelength description is only valid if we imagine that the pitch is fixed and the radius is allowed to go to infinity. In the limit where the radius is fixed and the pitch goes to zero the underlying lattice structure becomes important and a continuum theory is no longer appropriate.

Within the continuum theory, we note that this problem can be reduced to a lattice periodic problem in a twisted coordinate system that winds with the period of the external potential. We choose our coordinates so that the x -axis lies along the tube and the y -axis wraps around the circumference in a counterclockwise direction (in this way the y coordinate agrees with the usual azimuthal angle of radial coordinates). We let the nanotube radius be R and the pitch of the helix be c , as depicted in Fig. 1. The Dirac Hamiltonian in the presence of an external field becomes

$$H_K = -i\hbar v_f \vec{\sigma} \cdot \vec{\nabla} + V(x, y), \quad (1)$$

where v_f is the Fermi velocity, $\vec{\sigma} = \sigma_x \hat{x} + \sigma_y \hat{y}$ are the Pauli matrices, and $V(x, y)$ is the applied helical potential. The envelope function is subject to the quasi-periodic boundary condition $\Psi(x, y + 2\pi R) = \exp(2\pi i \delta) \Psi(x, y)$, where $\delta = \pm 1/3$ for semiconducting tubes and $\delta = 0$ for metallic tubes.^{12,13}

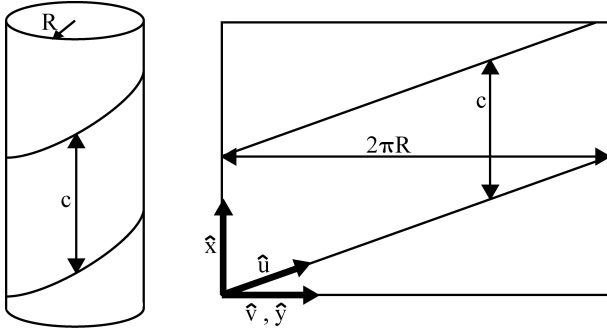


FIG. 1: The tube on the left illustrates the geometry of our model system. Here, R is the radius of the nanotube and c is the pitch of the helical potential. On the right is an “unwrapped” view of the nanotube surface, with the pitch and the nanotube circumference, $2\pi R$, marked. Also on the right are the four relevant spatial unit vectors for this system, the usual \hat{x} and \hat{y} of a Cartesian coordinate system and the non-orthogonal \hat{u} and \hat{v} used as a convenient basis in which to solve the Dirac equation in the presence of a helical potential.

The helical symmetry of the external potential implies that $V(x, y)$ is a function of the single variable $\omega = y/R \pm 2\pi x/c$, where the plus (minus) sign applies to left-handed (right-handed) helices, and $V(\omega + 2\pi) = V(\omega)$. We will capture the essential physics of the system by investigating the effects of the lowest Fourier mode of the potential. We let $V(x, y) = A \cos[(y - Px)/R]$, where A is the potential strength and $P = \pm 2\pi R/c$ is a convenient dimensionless parameter that characterizes the geometry of the helical potential, with $P > 0$ for right-handed helices and $P < 0$ for left-handed helices.

In Appendix A.1 we investigate the effects of higher Fourier terms and show that for the intravalley scattering considered below the higher Fourier terms are unimportant. However, higher Fourier terms can vary rapidly on the scale of a lattice constant, and rapidly varying potentials can lead to significant intervalley scattering.²⁰ Intervalley scattering involves a large momentum transfer and in general the Coulomb potential is unscreened at large momenta. Such an unscreened interaction gives higher order Fourier coefficients that are larger than the lowest screened Fourier coefficient, and we might expect that intervalley scattering will be at least as important as intravalley scattering. However, in Appendix A.2 we show that in general the intervalley scattering matrix elements are either kinematically forbidden or small compared with the first screened coefficient. In the very few cases where intervalley scattering may be important, we show that the matrix elements are about the same size as the intravalley elements and do not appreciably alter any of the results below.

The isotropy of the Dirac equation allows us to choose any two unit vectors as our basis vectors in the tangent plane of the tube. Here, it is convenient to take as a basis two unit vectors, \hat{u} and \hat{v} , such that \hat{u} points along an equipotential and \hat{v} follows the usual azimuthal coordi-

nate. Referring to Fig. 1, we see that

$$\begin{aligned}\hat{u} &= \frac{\hat{x}}{\sqrt{1+P^2}} + \frac{P\hat{y}}{\sqrt{1+P^2}}, \\ \hat{v} &= \hat{y}.\end{aligned}\quad (2)$$

With this choice of basis vectors a general vector in the plane is written as $\vec{r} = \hat{u}\hat{u} + \hat{v}\hat{v}$. The (u, v) coordinates may be obtained from the Cartesian (x, y) coordinates by

$$\begin{pmatrix} u \\ v \end{pmatrix} = \begin{pmatrix} \sqrt{1+P^2} & 0 \\ -P & 1 \end{pmatrix} \begin{pmatrix} x \\ y \end{pmatrix}.\quad (3)$$

In this basis the helical potential is a function of only the v coordinate, $V(v) = A \cos(v/R)$, and the Dirac equation becomes

$$\begin{aligned}-i\hbar v_f &\left(\sqrt{1+P^2} \sigma_x \partial_u + (\sigma_y - P\sigma_x) \partial_v \right) \Psi \\ &+ A \cos(v/R) \Psi = E \Psi.\end{aligned}\quad (4)$$

With this choice of spatial basis vectors we are forced to choose non-orthogonal reciprocal lattice basis vectors. We choose our reciprocal basis vectors, \vec{q}_u and \vec{q}_v , such that for a general wavevector, $\vec{k} = k_u \vec{q}_u + k_v \vec{q}_v$, the dot product with a general spatial vector is given by $\vec{k} \cdot \vec{r} = k_u u + k_v v$. This is accomplished using the reciprocal space (non-unit) vectors $\vec{q}_u = \sqrt{1+P^2} \hat{x}$ and $\vec{q}_v = -P \hat{x} + \hat{y}$. With this basis the (k_u, k_v) coordinates are obtained from the usual (k_x, k_y) coordinates by the transformation

$$\begin{pmatrix} k_u \\ k_v \end{pmatrix} = \frac{1}{\sqrt{1+P^2}} \begin{pmatrix} 1 & P \\ 0 & \sqrt{1+P^2} \end{pmatrix} \begin{pmatrix} k_x \\ k_y \end{pmatrix}.\quad (5)$$

If we now write $\Psi(u, v) = \exp(ik_u u) \psi(v)$, the Dirac equation becomes

$$\begin{aligned}\left(\sqrt{1+P^2} (k_u R) \sigma_x - iR(\sigma_y - P\sigma_x) \partial_v \right) \psi \\ + a \cos(v/R) \psi = \epsilon \psi,\end{aligned}\quad (6)$$

where $a = A/\Delta_0$ and $\epsilon = E/\Delta_0$ are dimensionless measures of the potential strength and the energy, respectively, and $\Delta_0 = \hbar v_f / R$ is a convenient unit of energy. The above Hamiltonian has the property that $H_K(-k_u, -P) = \sigma_y H_K(k_u, P) \sigma_y$, which shows that the spectrum satisfies $\epsilon(k_u, P) = \epsilon(-k_u, -P)$. We may therefore only consider right-handed helices and take $P \geq 0$ in all that follows.

When $P = 0$ Eq. (6) also describes a nanotube immersed in a constant perpendicular electric field, a system studied previously by Novikov and Levitov.^{21,22} They found that for semi-conducting tubes the band gap was unaffected by the applied field until a critical field strength was reached, above which the band gap closes. For metallic tubes there exists a critical field above which the Fermi velocity changes sign and the Fermi surface fractures. We will investigate similar effects for $P \neq 0$ below.

Novikov and Levitov used a chiral gauge transformation to show that, for the $P = 0$ system, the spectrum at $k_x = 0$ is unaffected by the applied field. For the $P \neq 0$ system we employ a similar transformation,

$$\mathcal{T} = \exp \left(ia(\sigma_y - P\sigma_x) \frac{\sin(v/R)}{\sqrt{1+P^2}} \right), \quad (7)$$

which converts the Hamiltonian to

$$\begin{aligned} H'_K &= TH_K T^{-1} \\ &= -iR(\sigma_y - P\sigma_x)\partial_v + \sqrt{1+P^2}(k_u R)\mathcal{T}\sigma_x\mathcal{T}^{-1}. \end{aligned} \quad (8)$$

Thus, the spectrum of Eq. (6) at $k_u = 0$ is unaffected by the applied helical potential.

When $k_u = 0$ solutions of Eq. (6) are of the form

$$\psi(v) = f(v) \begin{pmatrix} 1 \\ \pm \frac{P-i}{\sqrt{1+P^2}} \end{pmatrix} \exp \left(\pm i \frac{a \sin(v/R)}{\sqrt{1+P^2}} \right), \quad (9)$$

where $f(v)$ is independent of a . This shows that the applied field only alters the phase of the wavefunction at $k_u = 0$, and we use this fact to elucidate another protected quantity in the spectrum of Eq. (6). The k_u -space energy gradient is given by

$$\frac{\partial \epsilon}{\partial k_u} = \langle \psi | \frac{\partial H_K}{\partial k_u} | \psi \rangle, \quad (10)$$

provided both $\partial \epsilon / \partial k_u$ and $\partial |\psi\rangle / \partial k_u$ are well defined. Note that in general these derivatives are not well defined at degenerate points in the spectrum. For non-degenerate k_u points, if we write the wavefunction as

$$\psi(v) = \begin{pmatrix} \phi(v) \\ \theta(v) \end{pmatrix}, \quad (11)$$

then Eq. (10) becomes

$$\frac{\partial \epsilon}{\partial k_u} = R\sqrt{1+P^2} \int dv (\phi^* \theta + \theta^* \phi). \quad (12)$$

By Eq. (9), the right hand side is independent of a at $k_u = 0$, which shows that $\partial \epsilon / \partial k_u|_{k_u=0}$ is unaffected by the external helical potential. We therefore find that the longitudinal velocity, given by

$$v = \frac{1}{\hbar} \frac{\partial E}{\partial k_x} = \frac{\Delta_0}{\hbar\sqrt{1+P^2}} \frac{\partial \epsilon}{\partial k_u}, \quad (13)$$

is unaffected by the helical potential at $k_u = 0$.

III. SOLUTIONS

A. Zero Field Solutions

The helical band structure of Eq. (6) is different than that produced by the ordinary massless Dirac theory on

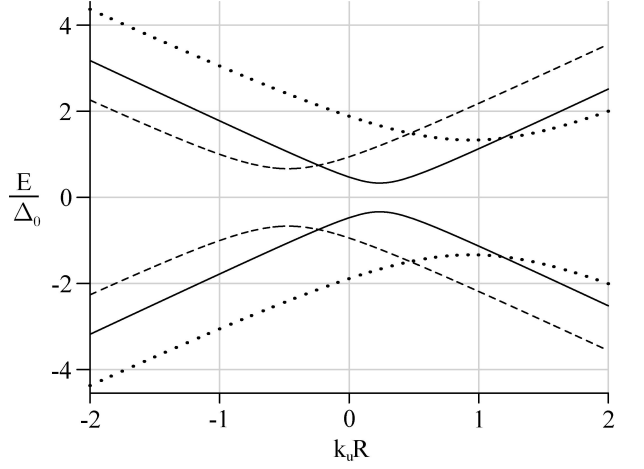


FIG. 2: The three highest valence bands and the three lowest conduction bands of a semiconducting nanotube ($\delta = 1/3$) plotted as a function of $k_u R$. The energy bands are plotted for a free nanotube ($a = 0$) studied in a twisted coordinate system appropriate for an applied potential with $P = 1$. The allowed energies, like all measurable quantities, are unaffected by the change in coordinate system. The apparent differences between this spectrum and the usual free nanotube spectrum, such as the shift in the location of band minima, arise because the energies are plotted as a function of $k_u R$, defined for the twisted coordinate system, and not the usual $k_x R$.

the cylinder both because of our choice of nonorthogonal coordinates and because of the applied helical potential. Only the latter change is physical, and in order to separate the two effects it is necessary to examine the field free solutions of Eq. (6). The appropriate boundary condition on $\psi(v)$ is obtained by noting that $\hat{v} = \hat{y}$, so that $\psi(v + 2\pi R) = \exp(2\pi i \delta) \psi(v)$. The field free energies are given by

$$\epsilon_{\alpha,m}^0 = \alpha \sqrt{\left[\sqrt{1+P^2}(k_u R) - P(m + \delta) \right]^2 + (m + \delta)^2}, \quad (14)$$

where the band index m is any integer and $\alpha = \pm 1$ denotes a conduction or valence band. The first few energy levels for a semiconducting CNT are plotted in Fig. 2. The band gaps, like all observable quantities, are unchanged by our choice of coordinate system. However, there are two noticeable differences when the free nanotube spectrum is plotted as a function of $k_u R$, defined for the twisted coordinate system, compared to the spectrum when plotted as a function of the usual $k_x R$. First, the band minima are shifted to positive (negative) k_u values for $m > 0$ ($m < 0$). The locations of the new band minima are given by $(k_u R)_{\min} = P(m + \delta) / \sqrt{1+P^2}$. Secondly, as $k_u R \rightarrow \infty$, the slope of each band goes as $\sqrt{1+P^2}$.

An intriguing feature of the band structure of semiconducting CNTs is that the bands are shifted so that the magnitude of the slope of all bands is the same at $k_u = 0$, namely $|\partial \epsilon_{\alpha,m} / \partial k_u|_{k_u=0} = PR$. As these

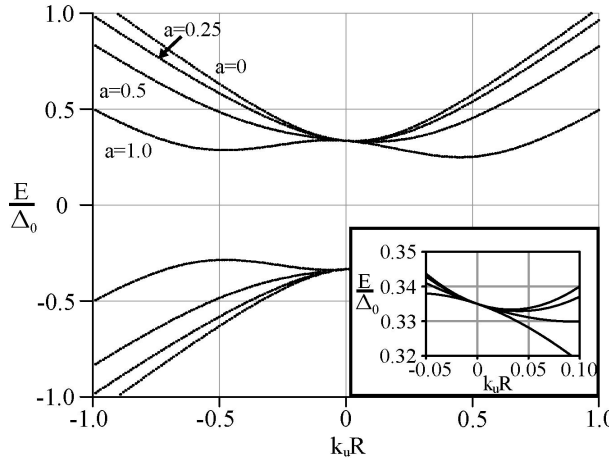


FIG. 3: The lowest conduction band and highest valence band as function of k_uR for a semi-conducting CNT with $\delta = 1/3$ and $P = 0.1$, drawn for several values of a as labeled in the figure. The inset is an expanded view of the lowest conduction bands in the area around $k_uR = 0$, and shows that the band gap closes for every non-zero a considered here.

are the protected locations in the spectrum, it is those states with $k_u = 0$ and with longitudinal velocity $v = \pm Pv_f/\sqrt{1+P^2}$ that are unaffected by the applied potential. The same holds true for the energy bands of metallic tubes except for the $m = 0$ bands. These bands, with energy $\epsilon_{\alpha,0} = \alpha\sqrt{1+P^2}(k_uR)$, remain degenerate at $k_u = 0$. From the analysis at the end of Sec. II, the slope of these bands may be changed by the applied field. These changes will be investigated below.

B. Non-zero Field Solutions

1. Semiconducting Nanotubes

The spectrum of Eq. (6) for semi-conducting nanotubes was determined numerically for many values of the field strength, a , and the dimensionless geometric parameter, P . A representative sample of results is shown in Figs. 3 - 5, where we plot the lowest conduction band and highest valence band for three different values of P and three different non-zero values of a . The most striking result of these solutions is that, unlike the $P = 0$ case, the band gap closes for any value of a . This is shown in the inset in Fig. 3 and will be confirmed analytically below. Although there is no critical field to be applied before the band gap closes, our results suggest that, at least for $P \lesssim 0.2$, there exists a critical field above which a second local minimum appears in the band structure. This is most clearly seen in Fig. 3, where the $a = 1.0$ band develops a second local minimum at about $k_uR = -0.48$. For larger P there is significant mixing of the $m = 0$ and $m = -1$ bands in the region where a second local minimum would develop, and the existence of

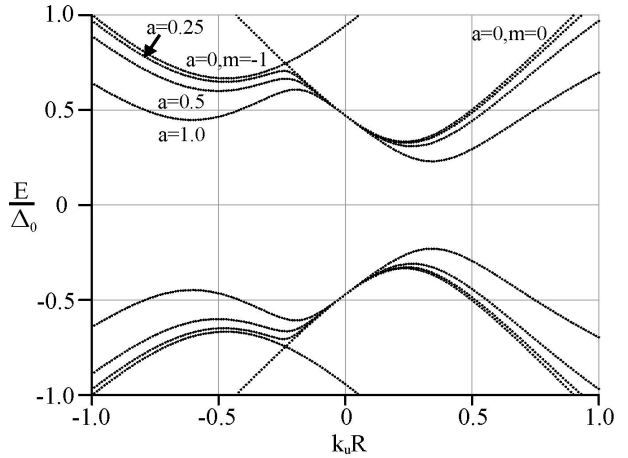


FIG. 4: The lowest conduction band and highest valence band as function of k_uR for a semi-conducting CNT with $\delta = 1/3$ and $P = 1.0$, drawn for several values of a as labeled in the figure.

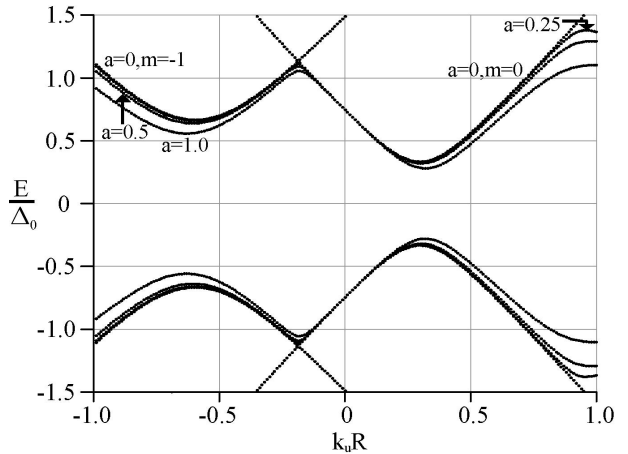


FIG. 5: The lowest conduction band and highest valence band as function of k_uR for a semi-conducting CNT with $\delta = 1/3$ and $P = 2.0$, drawn for several values of a as labeled in the figure.

a critical field in these cases is less certain. Nevertheless, for all values of a and $P > 0$ there exists only one global minimum. The location of the band minimum, $(k_uR)_{\min}$, increases as a increases.

The fractional change in the band gap is given by $F = [\Delta(P, a) - \Delta(P, 0)]/\Delta(P, 0)$, where $\Delta(P, a)$ is the minimum value of the conduction band for a given P and a , and $\Delta(P, 0) = 1/3$ is the minimum value of the unperturbed conduction band. F is plotted in Fig. 6 as a function of P for several values of a . For all a , F has a maximum for a P on the order of unity and decays relatively rapidly to zero as $P \rightarrow \infty$. This may also be seen by comparing Figs. 4 and 5, which show that doubling P significantly decreases the effect of the applied field. This behavior is most easily understood by considering the tight-binding model. The limit $P \rightarrow \infty$ corresponds

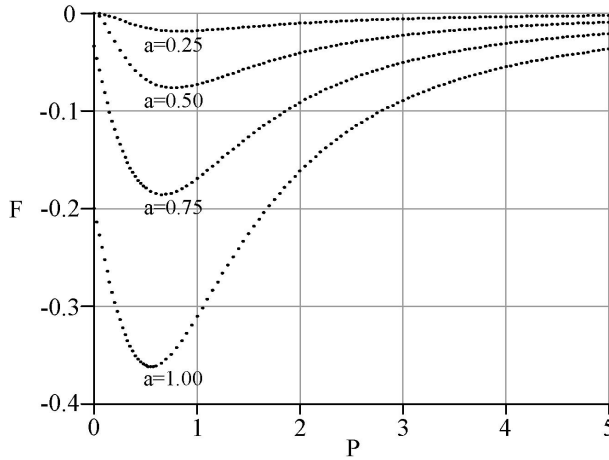


FIG. 6: The fractional change in the band gap, F , plotted as a function of P for several values of a . The band gap is unchanged as $P \rightarrow \infty$, as discussed in the text. As $P \rightarrow 0$ there are two behaviors: the band gap is unchanged if $a < a_c$, but closes for $a > a_c$. For all a there exists a P on the order of unity that produces the largest change in the band gap.

to taking the pitch to zero, at which point the helix collapses into a uniform cylinder. The potential is no longer spatially varying on the tube surface, and its only effect is to provide a uniform background potential. Such a uniform change may be eliminated by redefining the zero of energy, and thus cannot affect the band gap.

As $P \rightarrow 0$ the system asymptotically approaches the system studied by Novikov and Levitov, and their results apply. At $P = 0$ the band gap is unaffected by the applied field if $a \leq a_c \approx 0.6215$, and it closes if $a > a_c$. These two behaviors are evident in Fig. 6: for $a \leq a_c$, F rapidly approaches zero as $P \rightarrow 0$, while for $a > a_c$, F approaches an a -dependent constant less than zero.

To investigate the size of the band gap for small a we employ non-degenerate perturbation theory. The perturbation connects band (α, m) to bands $(\pm, m+1)$ and $(\pm, m-1)$, and the perturbed energies are given by

$$\epsilon_{\alpha,m} = \epsilon_{\alpha,m}^0 + \left(\frac{a}{2}\right)^2 \frac{G_m}{\epsilon_{\alpha,m}^0}, \quad (15)$$

where $\epsilon_{\alpha,m}^0$ is given by Eq. (14) and

$$G_m = \frac{4(k_u R)^2}{4 [P(k_u R) - \sqrt{1+P^2}(m+\delta)]^2 - (1+P^2)}. \quad (16)$$

Because of the many degeneracies in the spectrum at high energy (see Fig. 2), the effects of the chiral potential on the entire spectrum cannot be studied within a non-degenerate perturbation theory. However, there is never a degeneracy at the *band minimum* of the $m = 0$ band, and Eq. (15) accurately reproduces the band gaps found in numerical results. The fractional change in the band gap may be estimated by evaluating Eq. (15) at the

unperturbed band minimum, which gives

$$F_{\alpha,0} = \alpha \left(\frac{a}{2}\right)^2 \frac{4P^2|\delta|}{4\delta^2 - (1+P^2)^2}. \quad (17)$$

Notice that as $(1+P^2) > 2|\delta|$ for all P , the band gap always closes. The actual band gap is in fact slightly smaller than predicted by Eq. (17) because the unperturbed band minimum is not the true band minimum. Nevertheless, the conclusion that the band gap closes for any $a > 0$ remains valid.

To investigate the existence of a critical field and the development of a second local minimum we employ non-degenerate perturbation theory in small $k_u R$. The perturbation connects conduction bands to valence bands, and the perturbed energies are given by

$$\begin{aligned} \epsilon_{\alpha,m} = & \alpha|m+\delta|\sqrt{1+P^2} - \alpha \operatorname{sgn}(m+\delta)P(k_u R) \\ & + \alpha \operatorname{sgn}(m+\delta) \frac{(k_u R)^2 H_m}{\sqrt{1+P^2}}, \end{aligned} \quad (18)$$

where $\operatorname{sgn}(x)$ is the sign function and

$$H_m = \sum_{n=-\infty}^{\infty} J_n^2 \left(\frac{2a}{\sqrt{1+P^2}} \right) \frac{2(m+\delta)}{4(m+\delta)^2 - n^2}. \quad (19)$$

For $\delta = 1/3$, H_0 switches sign from positive to negative at $a_c \approx 0.6215\sqrt{1+P^2}$. For $a > a_c$ the curvature at $k_u = 0$ is negative and a second local minimum develops to the left of the origin, as deduced from the numerical results.

2. Metallic Tubes

The low energy spectrum of Eq. (6) for metallic tubes is shown in Figs. 7 and 8 for two different values of a and several values of P . As discovered by Novikov and Levitov, for $P = 0$, as the field is turned on the Fermi velocity decreases and the band acquires a non-zero curvature away from $k_u = 0$. The Fermi velocity goes to zero at a critical field strength, $a_{cm} \approx 1.203$. When $a > a_{cm}$ the Fermi velocity switches sign and the Fermi surface fractures, as shown in Fig. 8.

The spectrum for fixed $a < a_{cm}$ is plotted in Fig. 7 for several P values. As P increases the slope of the energy bands at $k_u = 0$ increases. However, note that as $v_f = \partial\epsilon/\partial k_x = (1/\sqrt{1+P^2})\partial\epsilon/\partial k_u$, the increase in the slope does not necessarily translate into an increase in the Fermi velocity. In fact, for very large P the slope increases linearly in P , which implies an unchanged Fermi velocity in the limit $P \rightarrow \infty$. This effect could have been anticipated from the analysis of the semiconducting band gap, where we argued that the effect of the chiral potential must disappear in the limit $P \rightarrow \infty$. As P increases the higher energy states mix with the $m = \pm 1$ bands and two symmetric local minima develop in the lowest band.

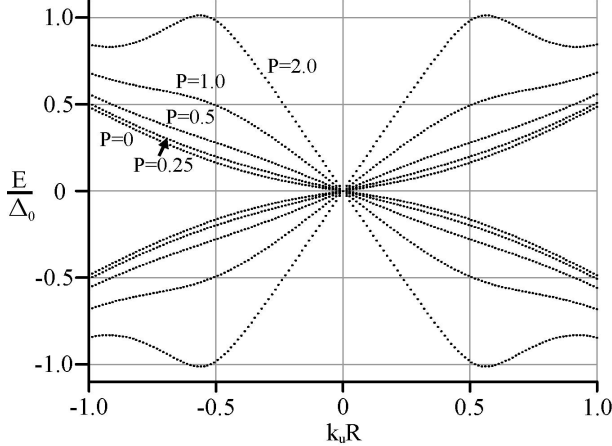


FIG. 7: The low energy bands of a metallic nanotube as a function of $k_u R$ for $a = 1.0 < a_{cm}$ for several values of P as labeled in the figure. The primary effect of the field is to modify the Fermi velocity.

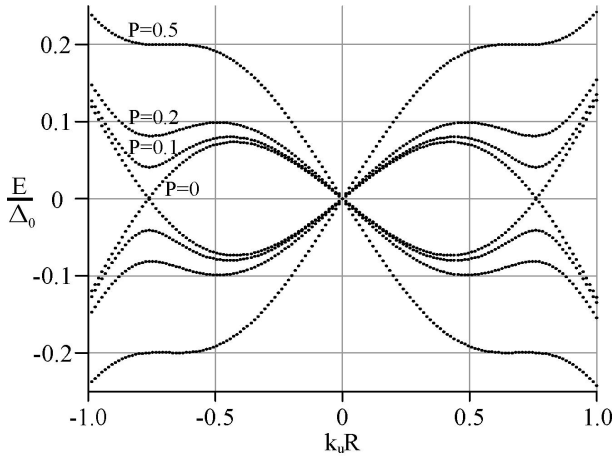


FIG. 8: The low energy bands of a metallic nanotube as a function of $k_u R$ for $a = 1.5 > a_{cm}$ for several values of P as labeled in the figure. For $P = 0$ the Fermi surface fractures, for $P > 0$ the Fermi surface is unchanged.

The spectrum for fixed $a > a_{cm}$ is plotted in Fig. 8, where it is seen that the effect of a non-zero P is to open up gaps where the $P = 0$ bands crossed the Fermi surface at non-zero k_u . For any $P > 0$ the Fermi surface does not fracture, and for this property $P = 0$ is a singular limit. As P increases the slope at $k_u = 0$ increases and the local minima at the induced band gaps at first flatten, then reappear as the lowest band begins to mix with the $m = \pm 1$ bands. As $P \rightarrow \infty$ the effects of the chiral potential disappear and the $a > a_{cm}$ system maps directly onto the $a < a_{cm}$ system.

We study the change in the Fermi velocity using degenerate perturbation theory on the two states at $k_u = 0$. The perturbed energies are given by

$$\epsilon_{\alpha,0} = \alpha \sqrt{P^2 + J_0^2 \left(2a/\sqrt{1+P^2} \right)} (k_u R). \quad (20)$$

For $P = 0$ the Fermi velocity vanishes when $2a = \mu_1 \approx 2.405$, the first zero of the Bessel function. When $P > 0$ the Fermi velocity is strictly non-zero. The slope of the bands is an oscillatory function of a , but as $J_0(x) \leq 1$, this oscillatory behavior will be small for large P . As $P \rightarrow \infty$ the slope goes as P , in agreement with the numerical results above.

IV. THE FIELD STRENGTH

To a first approximation, the DNA and polymers used to wrap nanotubes may be considered infinitely long, helically wrapped line charges. In order to estimate the magnitude of the field strength we model the wrapping molecule as a helical ribbon of width l , radius R_1 , and pitch c , with surface charge density σ_0 (see Fig. 9). The field strength is obtained by evaluating the leading Fourier coefficient of this charge configuration on the nanotube surface, $r = R$. At the end of this calculation we recover the line charge model by taking the limit $l \rightarrow 0$ with the linear charge density, $\lambda = l\sigma_0$, held fixed. In this section we work in SI units.

In a long wavelength theory of the applied fields, we break space into three macroscopic regions characterized by different dielectric constants, as shown in Fig. 9. Region 1, $r > R_1$, is composed of material outside the helical line charge, the aqueous solution or other solvent, or possibly vacuum. Region 2, $R_1 > r > R$, is composed of the material between the line charge and the nanotube, including DNA bases or uncharged regions of a wrapping polymer. Region 3, $R > r > 0$, is composed of the nanotube itself. Denote the dielectric constant in the i th region by ϵ_i .

The helical symmetry of the charge distribution implies that the potential can be expanded in cylindrical coordinates as

$$V_i(r, \phi, z) = B_0^{(i)} \ln(r/r_0^{(i)}) + \sum_{n=1}^{\infty} \left(A_n^{(i)} I_n(2\pi n r/c) + B_n^{(i)} K_n(2\pi n r/c) \right) \cos[n(\phi - 2\pi z/c)], \quad (21)$$

where $i = 1, 2, 3$ denotes the three regions of space and $A_n^{(i)}, B_n^{(i)}$, and $r_0^{(i)}$ are expansion coefficients to be determined. The coefficients are determined using the usual electrostatic boundary conditions,²³

$$V_>(r = r_i) = V_<(r = r_i), \\ \epsilon_> \frac{\partial V_>}{\partial r} \Big|_{r=r_i} - \epsilon_< \frac{\partial V_<}{\partial r} \Big|_{r=r_i} = -\sigma(r = r_i)/\epsilon_0, \quad (22)$$

where the boundary is located at $r = r_i$, $V_>$ and $\epsilon_>$ ($V_<$ and $\epsilon_<$) denote the potential and dielectric constant for $r \geq r_i$ ($r \leq r_i$), and σ is the charge density at the

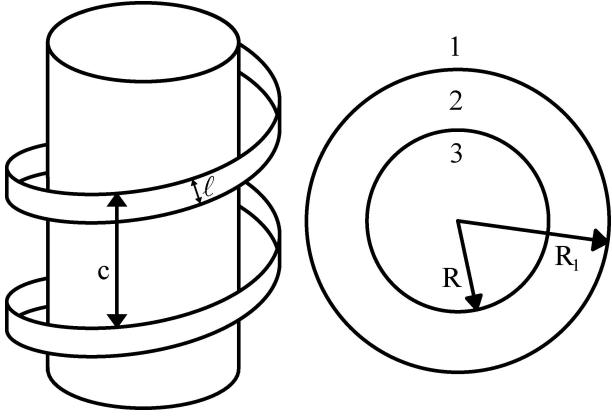


FIG. 9: On the left is a depiction of our model, a tube of radius R surrounded by a helical ribbon of radius R_1 , width l , and surface charge density σ_0 . On the right is a cross-sectional view of the system. The numbers refer to the three regions of space with different dielectric constants, as discussed in the text.

boundary. The charge density at $r = R_1$ is given by

$$\sigma(\phi, z) = \frac{x_0 \sigma_0}{c} + \sum_{n=1}^{\infty} \frac{2\sigma_0}{n\pi} \sin(n\pi x_0/c) \cos[n(\phi - 2\pi z/c)], \quad (23)$$

where $x_0 = l\sqrt{1 + P_1^2}/P_1$ and $P_1 = 2\pi R_1/c$.

The field strength is obtained from the Fourier expansion by $a = -eA_1^{(1)}I_1(P)/\Delta_0$, where the electron charge is $-e$. After taking the limit as the ribbon goes to a line charge, we find

$$a = \frac{e\lambda}{\pi\hbar v_f \epsilon_3 \epsilon_0} W(R_1, R) = CW(R_1, R), \quad (24)$$

where C is independent of R and R_1 , and

$$W = \left(\frac{\epsilon_3}{\epsilon_1} \right) \frac{R U(P_1, P)}{K_1'(P_1)S(P_1, P) - (\epsilon_2/\epsilon_1)K_1(P_1)T(P_1, P)}, \quad (25)$$

with

$$\begin{aligned} U(x, y) &= \frac{\sqrt{1 + x^2}}{x} \frac{K_1(x)I_1(y)}{1 - (\epsilon_3/\epsilon_2)} \left(\frac{K_1(y)}{I_1(y)} - \frac{K_1'(y)}{I_1'(y)} \right), \\ S(x, y) &= K_1(x) + \frac{I_1(x)}{1 - (\epsilon_3/\epsilon_2)} \left(\frac{\epsilon_3}{\epsilon_2} \frac{K_1(y)}{I_1(y)} - \frac{K_1'(y)}{I_1'(y)} \right), \\ T(x, y) &= K_1'(x) + \frac{I_1'(x)}{1 - (\epsilon_3/\epsilon_2)} \left(\frac{\epsilon_3}{\epsilon_2} \frac{K_1(y)}{I_1(y)} - \frac{K_1'(y)}{I_1'(y)} \right). \end{aligned} \quad (26)$$

To determine C we consider specifically the case of an ssDNA-CNT complex. The linear charge density of ssDNA is obtained by assuming each phosphate group on the backbone carries a charge of $-e$, which gives $\lambda \approx -1.5e/\text{nm}$. The dielectric constant of a CNT is obtained by using a result from Refs. (24) and (21), that when immersed in a perpendicular electric field the ratio of the field strength inside the tube to the applied

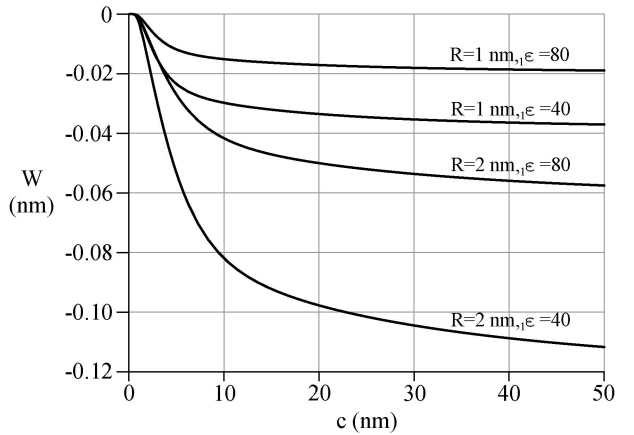


FIG. 10: The function $W(R, c, \epsilon_1)$ as a function of c for two values of R and two values of ϵ_1 .

field is given by $E/E_0 = 1/5$, independent of R . If the nanotube is modeled as a uniform solid cylinder with dielectric constant ϵ_3 then $E/E_0 = 2/(\epsilon_3 + 1)$, which gives $\epsilon_3 = 9$. Using these results and $v_f \approx 8 \times 10^5 \text{ m/s}$, we find $C \approx -1.8 \text{ nm}^{-1}$.

The distance between the ssDNA backbone and CNT surface is independent of nanotube radius, and is given by $R_1 - R \approx 0.6 \text{ nm}$. The dielectric constant for region 2 is difficult to approximate as it is composed of random DNA bases, solvent molecules and other dissolved species. However, provided the pitch is large compared to the nanotube radius the dominant screening effects should come from regions 1 and 3. We therefore ignore screening in region 2 and set $\epsilon_2 = 1$.

With these approximations $W = W(R, c, \epsilon_1)$. The asymptotic behavior of W for $R \gtrsim 1 \text{ nm}$ and $\epsilon_1 \gtrsim 5$ is $W \sim w_0 R/\epsilon_1$, where w_0 is a function of c . The behavior of W as a function of c is shown in Fig. 10 for two values of R and ϵ_1 . W goes to zero as $c \rightarrow 0$, and goes asymptotically to a constant value as $c \rightarrow \infty$. Physically realizable values of c are in the $1 - 60 \text{ nm}$ range,⁹ and in this region W is monotonically decreasing but its behavior is not given by a simple scaling relation.

To obtain an estimate of the field strength we use a CNT with $R = 0.5 \text{ nm}$ and a solution with $\epsilon_1 = 80$, which is approximately the dielectric constant of water. In Table I we calculate the field strength and the corresponding fractional change in the band gap for several values of the pitch. As c increases a asymptotically approaches 1.1×10^{-2} , while P monotonically decreases to zero. From Fig. 6 we expect the magnitude of F will be peaked for a P on the order of unity and decay to zero for very small and very large pitches. This behavior is confirmed in Table I, where $c = 5 \text{ nm}$ produces the largest change in the band gap. Notice that as the pitch increases the field strength continues to increase, but the corresponding decrease in P reduces the effect of the applied potential.

For the largest fractional change found here, the dif-

TABLE I: Calculated values of P , the field strength, a , and the fractional change in the band gap, F , for various values of the pitch, c . The other parameters of the system are described in the text.

c (nm)	P	a	F
1	3.14	6.6×10^{-4}	-3.6×10^{-8}
2	1.57	3.7×10^{-3}	-2.9×10^{-6}
5	0.63	7.6×10^{-3}	-1.5×10^{-5}
10	0.31	8.8×10^{-3}	-1.0×10^{-5}
25	0.13	1.0×10^{-2}	-2.7×10^{-6}
50	0.063	1.0×10^{-2}	-7.7×10^{-7}

ference between the original and perturbed band gap is about 0.01 meV. We do not expect a change of this scale to be readily measurable in transport or optical experiments. There are several possible ways one might consider to increase the size of this effect. The first is to use large radius nanotubes, which will increase the magnitude of the applied chiral potential. This approach has two problems. Fundamentally, as R is increased P is also increased, and the size of the effect decreases with increasing P . Practically, single-walled nanotubes are generally no larger than 1.0 nm in diameter, with larger radius tubes unstable to collapse.²⁵ The second method is to tune c so that for a given radius nanotube, P is slightly less than unity where the effect of the helical potential is largest. For shorter DNA strands a systematic study of pitch with varying bases is possible,⁷ but for a long DNA strand with hundreds or thousands of bases such a study is impractical. A third method is to change the wrapping polymer to one with a larger linear charge density or to one that rests closer to the nanotube surface. The linear charge density of DNA is already rather large and simply doubling or tripling the linear charge density will not increase the size of the effect enough for easy observation. The field strength increases exponentially as the charge approaches the nanotube surface, but the decay length is large relative to typical molecular distances. A fourth method is to change the environment of the DNA-CNT complex. The dielectric constant of water is unusually large and essentially reduces the field strength by a factor of 80. Most organic solvents have dielectric constants in the range 1–5, which would increase the field strengths calculated above by factors of 16–80. The DNA-CNT complex is remarkably stable, and it may be possible to create the complex in aqueous solution and then transfer it to an organic solvent. Other wrapping molecules have already been used to dissolve CNTs in organic solvents,^{15,26} and one of these might produce field strengths strong enough to produce a measurable effect.

V. CONCLUSION

We have investigated the effect of a helical potential on semi-conducting and metallic nanotubes. For semi-

conducting nanotubes the band gap closes for any non-zero field strength. The size of the effect is determined by both the field strength, a , and a dimensionless geometrical factor P , which is the ratio of the circumference of the nanotube to the pitch of the helix. For each a there exists an optimal P that produces the biggest change in the band gap. For metallic tubes, the helical potential decreases the Fermi velocity but does not fracture the Fermi surface. Under typical conditions the effect of the helical potential is probably unobservable, but we understand the scaling relationship between the size of the band gap and every control parameter, so in theory it is possible to design a system where these effects would be detectable in an optical experiment. In some ways the small size of the effect is encouraging, as it means that measurements on helically wrapped CNTs give results that are nearly identical to those of pristine CNTs. Also, a helically wrapped CNT can be substituted for a pristine CNT in almost any application, which may make device construction easier.

The theory developed here ignores higher order corrections, such as curvature effects and higher Fourier terms in the potential. Simply expanding the tight-binding graphene Hamiltonian to the next lowest gradient order generates terms that break the chiral gauge symmetry and introduce a correction to the spectrum at $k_u = 0$. Such corrections will modify the functional form of our analytic expressions; for example, curvature effects will introduce a chiral angle dependent band gap. However, curvature effects and higher order expansion terms introduce corrections that are small compared to the energies of interest. The theory developed here also ignores exciton effects, which are known to be large in CNTs. Exciton effects in optical experiments may alter the numerical values obtained here by 20–30%, but they should not significantly change our general results or alter the conclusions outlined in the previous paragraph.

This work was supported by the Department of Energy under grant DE-FG-84ER45118.

APPENDIX A: HIGHER FOURIER COEFFICIENTS

A general chiral potential on the nanotube may be written as

$$V(\vec{r}) = \sum_{n=1}^{\infty} V_n \cos(\vec{Q}_n \cdot \vec{r}), \quad (A1)$$

where $\vec{Q}_n = \pm 2\pi n/c \hat{x} + n/R \hat{y}$. In our calculations above we only retained the first Fourier term in order to capture the essential physics of the system. In this Appendix we investigate the effect of including the higher Fourier terms in the Hamiltonian. Our perturbation calculations above only included contributions from intravalley scattering matrix elements, specifically, scattering from a state near the \mathbf{K} point to another state near the \mathbf{K} point.

TABLE II: Calculated values of higher field strength Fourier coefficients for the nanotube system studied in Sec. IV.

c (nm)	a_1	a_2/a_1	a_3/a_1	a_4/a_1
2	0.0037	0.063	5.4×10^{-3}	5.2×10^{-4}
5	0.0075	0.16	3.7×10^{-2}	9.5×10^{-3}
10	0.0088	0.20	5.6×10^{-2}	1.8×10^{-2}
50	0.0104	0.20	5.9×10^{-2}	2.0×10^{-2}

In section A.1 we show that in all cases higher Fourier coefficients add a negligible correction to the intravalley matrix elements.

The higher Fourier terms vary rapidly on the scale of a lattice constant and contribute to scattering with a large momentum transfer. Such scattering may connect states at \mathbf{K} with those at \mathbf{K}' , so we must also consider intervalley scattering matrix elements in our perturbation expansion. At large momentum transfer the Coulomb interaction is unscreened and the Fourier coefficients in Eq. (A1) will be significantly larger than the corresponding screened coefficients. Nevertheless, we show in section A.2 that in almost all cases the intervalley scattering matrix elements can be neglected compared to the intravalley scattering matrix elements. In a few systems with small radius nanotubes, the intervalley matrix elements may be nearly as large as the intravalley scattering matrix elements. We discuss these few cases below.

1. Intravalley Scattering

The dimensionless potential energy appearing in the Hamiltonian is given by

$$U(\vec{r}) = \sum_{n=1}^{\infty} a_n \cos(\vec{Q}_n \cdot \vec{r}), \quad (\text{A2})$$

where $a_n = -eV_n/\Delta_0$. The coefficient a_1 was evaluated in Sec. IV. The n th Fourier coefficient is obtained in the same manner and is given by equations very similar to Eqs. (24 - 26), but involving $I_n(nx)$ and $K_n(nx)$ instead of $I_1(x)$ and $K_1(x)$. If this full potential is used to calculate the intravalley matrix elements, then the n th Fourier term connects the $m = 0$ band to the $m = \pm n$ bands. When squared and summed to obtain the second order perturbation to the energy, all of the cross terms vanish and we are left with

$$\begin{aligned} \Delta^{(2)} &= c_1 a_1^2 + c_2 a_2^2 + c_3 a_3^2 + \dots \\ &\approx c_1 a_1^2 [1 + (a_2/a_1)^2/2 + (a_3/a_1)^2/3 + \dots], \end{aligned} \quad (\text{A3})$$

where the c_i are constants (independent of the field strength) and we have approximated $c_n \approx c_1/n$, the factor of $1/n$ coming from the energy denominator. In Table II we list a_i/a_1 , for $i = 2 - 4$, for the DNA-CNT system studied in Sec. IV. Using $a_2/a_1 \lesssim 0.2$, we find that including the second Fourier term only changes the second order energy shift by about 2%. The energy shift was already much less than the unperturbed energy, and a 2% change to such a small shift can obviously be neglected.

2. Intervalley Scattering

The effects of intervalley scattering can be included with an effective Hamiltonian derived in Ref. (20),

$$H_{\text{eff}} = \begin{pmatrix} u_A(r) & -i\hbar v_f (\partial_x - i\partial_y) & -\omega e^{i\theta} \tilde{u}_A^*(r) & 0 \\ -i\hbar v_f (\partial_x + i\partial_y) & u_B(r) & 0 & e^{-i\theta} \tilde{u}_B^*(r) \\ -\omega^* e^{-i\theta} \tilde{u}_A(r) & 0 & u_A(r) & -i\hbar v_f (\partial_x + i\partial_y) \\ 0 & e^{i\theta} \tilde{u}_B(r) & -i\hbar v_f (\partial_x - i\partial_y) & u_B(r) \end{pmatrix}, \quad (\text{A4})$$

where the states are written in the $KA, KB, K'A, K'B$ basis, θ is the chiral angle, and $\omega = \exp(2\pi i/3)$. The

effective potentials in Eq. (A4) are given by

$$\begin{aligned} u_A(\vec{r}) &= \sum_{R_A} g(\vec{r} - \vec{R}_A) U(\vec{R}_A), \\ u_B(\vec{r}) &= \sum_{R_B} g(\vec{r} - \vec{R}_B) U(\vec{R}_B), \\ \tilde{u}_A(\vec{r}) &= \sum_{R_A} g(\vec{r} - \vec{R}_A) e^{i(\vec{K} - \vec{K}') \cdot \vec{R}_A} U(\vec{R}_A), \\ \tilde{u}_B(\vec{r}) &= \sum_{R_B} g(\vec{r} - \vec{R}_B) e^{i(\vec{K} - \vec{K}') \cdot \vec{R}_B} U(\vec{R}_B), \end{aligned} \quad (\text{A5})$$

TABLE III: Calculated ratios of the n th unscreened Fourier coefficient to the first screened Fourier coefficient for the nanotube system studied in Sec. IV.

c (nm)	$a_1^{(u)}/a_1^{(s)}$	$a_2^{(u)}/a_1^{(s)}$	$a_3^{(u)}/a_1^{(s)}$	$a_4^{(u)}/a_1^{(s)}$	$a_5^{(u)}/a_1^{(s)}$	$a_6^{(u)}/a_1^{(s)}$	$a_7^{(u)}/a_1^{(s)}$
2	190	13	1.1	0.10	1.1×10^{-2}	1.2×10^{-3}	1.3×10^{-4}
5	200	35	7.8	2.0	0.52	0.15	4.2×10^{-2}
10	190	41	12	3.6	1.2	0.42	0.15
50	170	40	12	4.0	1.5	0.56	0.22

where $U(\vec{r})$ is given by Eq. (A2), $\vec{R}_A = \vec{R} + \vec{\tau}_A$ ($\vec{R}_B = \vec{R} + \vec{\tau}_B$) denotes a site on the A (B) sublattice, and $g(\vec{r} - \vec{R})$ is a function peaked at R with a width of about a lattice constant and normalized so that $\sum_R g(\vec{R}) = 1$. The effective potentials contain information about the external chiral potential and the underlying graphene lattice, and in general do not share the same symmetry as the applied potential. Furthermore, u_i and \tilde{u}_i do not share the same symmetry, and there is no coordinate transformation analogous to Eqs. (2) and (3) to express these potentials in terms of a single variable.

Second order perturbation theory shows that the off-diagonal matrix elements contribute in the same way as the diagonal matrix elements (that is, we have to compute $|\langle K|\tilde{u}|K'\rangle|^2/(E_K - E_{K'})$). Thus, to get an estimate for the energy shift due to the off-diagonal terms we need only calculate the largest Fourier coefficient of those terms. As mentioned in Sec. II, the Coulomb potential is nearly unscreened at high momentum transfer, and the unscreened Fourier coefficients of the potential can be much larger than the screened coefficients. In Table III we list $a_n^{(u)}/a_1^{(s)}$, the ratio of the n th unscreened Fourier coefficient to the first screened Fourier coefficient, for the nanotube system studied in Sec. IV. From the size of the coefficients it appears intervalley scattering could be more important than intravalley scattering.

The off-diagonal matrix elements are evaluated as

$$\langle K, k_x, m | \tilde{u}_i | K', k'_x, n \rangle \propto \sum_{n \neq 0} a_n \sum_G \delta_{\vec{p} - \vec{Q}_n + \vec{K} - \vec{K}', \vec{G}} \quad (A6)$$

where $\vec{p} = (k_x - k'_x)\hat{x} + (m - n + 2\delta)/R \hat{y}$, the sum on n is over all integers except 0, and the sum on G is over all reciprocal lattice vectors of the graphene lattice. This may be rewritten as

$$\langle K, k_x, m | \tilde{u}_i | K', k'_x, n \rangle \propto \sum_{n \neq 0} a_n \sum_{K'_i} \delta_{\vec{p} - \vec{Q}_n, \vec{K}'_i} \quad (A7)$$

where the sum is over all K' points in reciprocal space. Because of the magnitudes of \vec{p} and \vec{Q}_n , only the K' points on the edge of the first Brillouin may contribute to this sum. These points are a function of the chiral

angle and are given by

$$\begin{aligned} \vec{K}'_1 &= \frac{2\pi}{3a} \left\{ (\cos \theta + \sqrt{3} \sin \theta) \hat{x} + (\sqrt{3} \cos \theta - \sin \theta) \hat{y} \right\} \\ \vec{K}'_2 &= \frac{2\pi}{3a} \left\{ (\cos \theta - \sqrt{3} \sin \theta) \hat{x} - (\sin \theta + \sqrt{3} \cos \theta) \hat{y} \right\} \\ \vec{K}'_3 &= -\frac{4\pi}{3a} \cos \theta \hat{x} + \frac{4\pi}{3a} \sin \theta \hat{y}. \end{aligned} \quad (A8)$$

To remain in the low energy regime we require $|\vec{p}| \lesssim 1/a$, which implies that the only terms contributing to the sum in Eq. (A7) will have

$$|\vec{Q}_n - \vec{K}'_i| \lesssim 1/a. \quad (A9)$$

The expression on the left-hand side of Eq. (A9) depends on n , c , R , θ , and on the particular choice of K' point. We undertook a systematic search of the relevant parameter space to determine when Eq. (A9) was satisfied. The search was limited to $-6 \leq n \leq 6$ because it is clear from Table III that the coefficients of higher Fourier terms will always be negligible. Preliminary investigations showed it was sufficient to restrict the chiral angle to $\theta = 0, \pm\pi/12$ or $\pm\pi/6$. For each of these 180 cases we plotted $|\vec{Q}_n - \vec{K}'_i|$ as a function of c and R to find where the inequality (A9) is satisfied. The search was restricted to physical values of the pitch and the radius, $1 \text{ nm} \leq c \leq 60 \text{ nm}$ and $0.3 \text{ nm} \leq R \leq 1.0 \text{ nm}$. We found 26 cases where there was any region in the (c, R) plane where the inequality was satisfied.

For each of these regions we evaluated the ratio $a_n^{(u)}/a_1^{(s)}$ to determine if the size of the intervalley scattering matrix element is comparable to the size of the intravalley scattering matrix element. As a conservative estimate the ratio was considered significant if

$$a_n^{(u)}/a_1^{(s)} \geq 0.75. \quad (A10)$$

There are 7 cases where the intervalley matrix element is kinematically allowed (inequality (A9) is satisfied) and the unscreened coefficient is large enough to be considered significant. These 7 cases are listed in Table IV, where it is seen that both inequalities are satisfied only for very small radius nanotubes, and then only in a narrow range of radii. Likewise, the pitch must generally be restricted to a narrow range. In an arbitrary sample of nanotubes the fraction of tubes that satisfy such restrictions will be small, and the intravalley scattering

TABLE IV: This table shows the 7 cases where both inequalities (A9) and (A10) are satisfied. The range of c and R over which the inequalities are satisfied is given, along with the ratio of the unscreened coefficient to the screened coefficient and the fractional change in the energy shift. In the first column i refers to a specific K'_i point.

i	n	θ	Range of c (nm)	Range of R (nm)	a_n^u/a_1^s	$(a_n^u/a_1^s)^2/ n $
1	3	$\pi/12$	1.9 – 2.2	0.30 – 0.35	0.75 – 1.2	0.19 – 0.48
1	4	$-\pi/12$	3 – 13	0.30 – 0.32	0.75 – 1.75	0.14 – 0.76
1	4	0	4 – 5.5	0.30 – 0.33	0.75 – 1.3	0.14 – 0.42
1	5	$-\pi/6$	unrestricted	0.37 – 0.38	0.75 – 0.90	0.11 – 0.16
1	5	$-\pi/12$	15 – 20	0.37 – 0.38	0.75 – 0.80	0.11 – 0.13
2	-4	$\pi/6$	> 20	0.30 – 0.31	~ 1.75	~ 0.76
2	-5	$\pi/6$	> 15	0.37 – 0.38	0.75 – 0.80	0.11 – 0.13

effects will dominate the intervalley scattering effects in any measurement.

It may be possible to prepare a sample in one of the allowed regions in Table IV, but even then intervalley effects will be no more important than the intravalley scattering already calculated. The energy shifts due to intravalley scattering are so small compared to the unperturbed energy that adding an additional shift of the same order of magnitude will not make the effects of a

chiral potential any easier to observe. Furthermore, the additional shifts due to intervalley scattering are small enough that they do not alter any of the conclusions from the main body of the paper. Lastly, note that these results were calculated assuming no screening. If there is any residual screening either by the nanotube or by the environment, then the shifts due to intervalley scattering will be further suppressed.

- ¹ M. J. O'Connell, P. Boul, L. M. Ericson, C. Huffman, Y. Wang, E. Haroz, C. Kuper, J. Tour, K. D. Ausman, and R. E. Smalley, *Chem. Phys. Lett.* **342**, 265 (2001).
- ² M. Zheng, A. Jagota, E. D. Semke, B. A. Diner, R. S. McLean, S. R. Lustig, R. E. Richardson, and N. G. Tassi, *Nature Mater.* **2**, 338 (2003).
- ³ V. C. Moore, M. S. Strano, E. H. Haroz, R. H. Hauge, and R. E. Smalley, *Nano Lett.* **3**, 1379 (2003).
- ⁴ H. Gao and Y. Kong, *Annu. Rev. Mater. Res.* **34**, 123 (2004).
- ⁵ M. S. Arnold, S. I. Stupp, and M. C. Hersam, *Nano Lett.* **5**, 713 (2005).
- ⁶ D. A. Heller, S. Baik, T. E. Eurell, and M. S. Strano, *Adv. Mater.* **17**, 2793 (2005).
- ⁷ M. Zheng, A. Jagota, M. S. Strano, A. P. Santos, P. Barone, S. G. Chou, B. A. Diner, M. S. Dresselhaus, R. S. McLean, G. B. Onoa, et al., *Nature* **302**, 1545 (2003).
- ⁸ A. Star, D. W. Steuerman, J. R. Heath, and J. F. Stoddart, *Angew. Chem. Int. Ed.* **41**, 2508 (2002).
- ⁹ B. Gigliotti, B. Sakizzie, D. S. Bethune, R. M. Shelby, and J. N. Cha, *Nano Lett.* **6**, 159 (2006).
- ¹⁰ M. S. Arnold, A. A. Green, J. F. Hulvat, S. I. Stupp, and M. C. Hersam, *Nature Nanotech.* **1**, 60 (2006).
- ¹¹ A. Wall and M. S. Ferreira, *Phys. Rev. B* **74**, 233401 (2006).
- ¹² H. Ajiki and T. Ando, *J. Phys. Soc. Jpn.* **62**, 1255 (1993).
- ¹³ C. L. Kane and E. J. Mele, *Phys. Rev. Lett.* **78**, 1932 (1997).
- ¹⁴ V. I. Puller and S. V. Rotkin, *Europhys. Lett.* **77**, 27006 (2007).
- ¹⁵ R. Czerw, Z. Guo, P. M. Ajayan, Y.-P. Sun, and D. L. Carroll, *Nano Lett.* **1**, 423 (2001).
- ¹⁶ J. N. Coleman and M. S. Ferreira, *Appl. Phys. Lett.* **84**, 798 (2004).
- ¹⁷ G. Dukovic, M. Balaz, P. Doak, N. D. Berova, M. Zheng, R. S. Mclean, and L. E. Brus, *J. Am. Chem. Soc.* **128**, 9004 (2006).
- ¹⁸ S. Meng, P. Maragakis, C. Papaloukas, and E. Kaxiras, *Nano Lett.* **7**, 45 (2007).
- ¹⁹ D. R. Hofstadter, *Phys. Rev. B* **14**, 2239 (1976).
- ²⁰ T. Ando and T. Nakanishi, *J. Phys. Soc. Jpn.* **67**, 1704 (1998).
- ²¹ D. S. Novikov and L. S. Levitov, *Phys. Rev. Lett.* **96**, 036402 (2006).
- ²² D. S. Novikov and L. S. Levitov, *arxiv:cond-mat/0204499* (2002).
- ²³ D. J. Griffiths, *Introduction to Electrodynamics* (Prentice-Hall, 1999), 3rd ed., ISBN 0-13-805326-X.
- ²⁴ L. X. Benedict, S. G. Louie, and M. L. Cohen, *Phys. Rev. B* **52**, 8541 (1995).
- ²⁵ G. Gao, T. Çağın, and W. A. Goddard III, *Nanotechnology* **9**, 184 (1998).
- ²⁶ A. Star, J. F. Stoddart, D. Steuerman, M. Diehl, A. Boukai, E. W. Wong, X. Yang, S.-W. Chung, H. Choi, and J. R. Heath, *Angew. Chem. Int. Ed.* **40**, 1721 (2001).